https://doi.org/10.1016/j.jpowsour.2023.232995

An advanced organic cathode for non-aqueous and aqueous calcium-based dual ion batteries

Rui Zhou[a], Zhen Hou[a], Ke Fan[a], Ching Kit Wun[b], Qun Liu[a], Tsz Woon Benedict Lo[a,b]
Haitao Huang[a,]* and Biao Zhang[a,]*

[a] *Department of Applied Physics, The Hong Kong Polytechnic University, 11 Yuk Choi Road, Hung Hom, Hong Kong, China.*
[b] *Department of Applied Biology and Chemical Technology, The Hong Kong Polytechnic University, 11 Yuk Choi Road, Hung Hom, Hong Kong, China.*

*Corresponding author.
E-mail address: biao.ap.zhang@polyu.edu.hk (Biao Zhang); haitao.huang@polyu.edu.hk (Haitao Huang)

ABSTRACT

The development of calcium batteries remains a grand challenge because of the lack of appropriate cathodes and electrolytes as well as their compatibility with promising anodes. Herein, we probe the electrolyte chemistry for realizing an advanced organic polymer cathode, polytriphenylamine (PTPAn), and demonstrate the potential of building reliable Ca-based dual ion batteries in both organic and aqueous electrolytes. Complementary experimental and theoretical studies reveal that the cathode reaction mechanism lies in the reversible combination/release of anions with N active sites in PTPAn, leading to a capacity of 88 mAh g^{-1} with an average voltage of 3.8 V (vs. Ca/Ca^{2+}) at 0.1 A g^{-1}. Coupling with a graphite anode in $Ca(TFSI)_2$/tetraglyme electrolytes, the graphite|PTPAn full cell shows a decent voltage of 2.45 V. It exhibits superior stability of over 2000 cycles with extremely fast kinetics up to 50C rate. Interestingly, PTPAn is also highly compatible with 6.25 M $Ca(TFSI)_2/H_2O$ electrolytes, allowing the construction of an all-organic aqueous calcium-based dual ion battery by coupling with a 3,4,9,10-perylene-tetracarboxylic-diimide anode. This study demonstrates the potential of building ultra-stable Ca batteries through anion-hosting cathodes coupled with customized electrolyte chemistry.

Keywords: Calcium batteries; Cathode; Anion combination/release; Non-aqueous; Aqueous.

1. Introduction

Lithium ion batteries (LIBs) have been widely used in our daily life, such as portable electronic devices and electric vehicle. However, the scarcity of lithium sources limits the development of LIBs as a large-scale energy storage system. Na and K ion batteries can circumvent this challenge due to their abundant reserves, but their higher redox potentials inevitably lead to the reduced energy density [1-5]. Different from these monovalent ion batteries, multivalent ion batteries (i.e., Ca, Mg, Al), possessing multi-electron redox chemistry, are regarded as promising candidates to bring about potential energy benefits [6,7]. In particular, Ca-based batteries are prized for natural abundance of Ca element and lower redox potential of Ca/Ca^{2+} (-2.87 V vs. standard hydrogen electrode) than other metal (-2.37 V of Mg/Mg^{2+}, -1.66 V of Al/Al^{3+}, -0.76 V of Zn/Zn^{2+}) [8-10], beneficial to achieving high-voltage full battery [11,12]. At the current stage, the development is significantly hindered by lacking suitable electrodes [13-19]. The formation of Ca^{2+}-blocking solid electrolyte interphase restricts the Ca metal anode design, which has been partly resolved through the electrolyte formulation optimizations and the utilization of Ca^{2+}-intercalation graphite anode as well as most recent reported Ca-tin composite strategy [20-29]. Turning to the cathodes, most of the candidates are derived from the Li-based analogs, but they suffer partly from poor cyclic stability and rate capability due to the accelerated structural degradation and the sluggish diffusion kinetics induced by large ionic radius and divalent Ca^{2+} [30-45]. More critically, the distinct electrolytes required for the cathodes and anodes make the construction of stable and high-voltage calcium batteries a great challenge.

Ca-based dual ion batteries (CDIBs) employing an anion storage cathode are promising to circumvent the above issues since the anion insertion is characteristic of good reversibility, fast kinetics and high operating voltage [46]. Nevertheless, the anion insertion cathode has rarely been investigated in CDIBs systems except for graphite material. Tang's group demonstrates that the PF_6^- anion can be reversibly intercalated/de-intercalated into graphite cathode, giving an exceptional capacity of ~75 mAh g^{-1} for over 350 cycles [47-49]. The anion intercalation at high voltages (up to 5 V) in graphite cathode inevitably triggers the electrolyte decomposition, necessitating further improvements by designing stable cathode-electrolyte interphase. Organic compounds, such as polytriphenylamine (PTPAn) and polyaniline, are also attractive candidates for hosting anions. Their flexible framework allows reversible anion uptake at rapid kinetics without significant structural deformation [50]. Although PTPAn material has been reported as the cathode for alkali-metal batteries, a simple extrapolation from mono- to multiple-valence ion battery systems is not sufficient because of the distinct salt/solvent chemistry that also plays a crucial role [29]. This is evidenced by the brief comparison between Li and Ca systems (Fig. S1). Furthermore, Wu's group reports several exceptional polyimides-based anodes and matches them with the PTPAn cathode to fabricate a 0.9 V CDIB in

$Ca(ClO_4)_2$/acetonitrile electrolyte [51]. Nevertheless, the incompatibility of acetonitrile-based electrolyte with low-potential anodes limits the energy density of the cell. Moreover, the detailed anion insertion chemistry in PTPAn remains largely unexplored.

Because of the poor reversibility of Ca metal and alloy anodes at this stage, graphite is almost the sole candidate accepting Ca^{2+} at an appropriate potential of 0.7 V with decent Coulombic efficiency (CE) during cycling. Graphite anode is only possible through solvent co-intercalation, curbing the electrolytes to very limited candidates, such as tetraglyme (G_4) and dimethylacetamide (DMAc)-derived ones [27,28]. Considering the poor oxidation stability of DMAc, we focus on the G_4 solvent and investigate anion effect (i.e., BF_4^-, FSI^- and $TFSI^-$) on the electrochemical behavior in PTPAn cathode for building high-voltage and ultra-stable CDIBs. It is observed that electrochemical performance is highly related to anion types owing to distinct diffusion energy barriers and binding energies. The reversible redox process between C-N and positively charged $C{=}N^+$ during the charge/discharge process is responsible for the capturing/releasing of anions, as revealed by the complementary physicochemical characterizations and theoretical calculations. The graphite|PTPAn CDIB in $Ca(TFSI)_2$ electrolyte delivers a 2.45 V output voltage with a superior rate capability (50C rate, 1C = 0.1 A g^{-1}) and long-term cycle stability (2000 cycles) at both 25 and 0 °C. Considering the appropriate redox potential of the PTPAn, we extend the study to the aqueous electrolytes by coupling with an organic anode, demonstrating the potential to build sustainable and high-safety aqueous CDIBs.

2. Experimental

2.1. Synthesis of PTPAn

PTPAn powders were synthesized by polymerizing triphenylamine (TPA) under an Ar atmosphere. Specifically, a total of 0.1 mol $FeCl_3$ (0.025 mol for every hour) was added into 100 mL 0.25 M of TPA-chloroform ($CHCl_3$) dispersed solution. After 4-hour reaction, 50 mL of methanol were introduced into the mixture to deposit the PTPAn powders, followed by filtration and washing with methanol three times. The resultant products were further purified through re-dissolving in $CHCl_3$ to filtrate insoluble impurities. The final PTPAn powders were obtained by adding a mixture of acetone and 5% aqueous ammonia into the remaining filtrate, filtrating and drying the precipitation at 40 ^oC under vacuum.

2.2. Preparation of electrodes

Aluminum foil (20 μm, 99.6%), copper foil (22 μm, 99.99%) and stainless-steel foil (30 μm) are purchased from Canrd Technology Co., Ltd. A slurry containing 60% PTPAn powder, 30% acetylene blacks and 10% poly(1,1-difluoroethylene) (PVDF) in N-methyl pyrrolidone (NMP) was cast onto Al foil and dried at 80 ^oC under vacuum for 12 h. The average mass loading of the PTPAn electrode is about 0.8 mg cm^{-2} and the thickness is 72 μm, the apparent electrode density is 0.11 g cm^{-3}. Graphite (KS6 from Timrex) and PTCDI (Aldrich) were mixed with acetylene blacks and PVDF in the mass ration of 90:5:5 and 5:3:2, dispersed in NMP to form slurries for preparing the corresponding electrodes. The obtained graphite slurry was then cast onto Cu foil, while PTCDI slurry was cast onto a stainless-steel foil and dried at 80 ^oC under vacuum. The average mass loading and thickness of the as-prepared graphite electrode are about 2 mg cm^{-2} and 129 μm, respectively. The PTCDI film can be easily peeled from stainless-steel foil to form a freestanding electrode. The average mass loading of PTCDI electrode is 0.8 mg cm^{-2} and its thickness is 114 μm. The diameters of all electrodes in this work are 12 mm.

2.3. Characterizations

The morphologies of PTPAn powders and electrodes were obtained using scanning electron microscopy (SEM, TESCAN MAIA3) and transmission electron microscopy (TEM, JEOL 2010F). Raman spectra were collected by a Witec-Confocal Raman system (UHTS 600 SMFC VIS) using an excitation wavelength of 532 nm. The XRD patterns and XPS spectra of obtained materials were respectively acquired with the Rigaku Smartlab diffractometer and Termo Scientific K-Alpha X-ray photoelectron spectrometer system. For the ex-situ Raman and XPS test, coin cells are disassembled in a glovebox after charging/discharging to specific states. The XPS samples were washed by G_4 solvent and sealed in a vacuum transfer holder to avoid air exposure. Attenuated total reflection-Fourier transform infrared spectroscopy (ATR-FTIR) spectra were recorded with the Nicolet IS50 FTIR spectrometer. Solid-state ^{19}F magic angle spinning (MAS) NMR experiments were performed on Bruker 600 MHz spectrometer (AVANCE NEO) at a Larmor frequency of 564.79 MHz in a 3.2 mm probe. The spinning rate was set as 16 kHz for all measurements. A single pulse with length of 2.65 μs was used for polarizing ^{19}F magnetization. The spectra were calibrated to ammonium trifluoroacetate powder at -74.6 ppm.

2.4. Electrochemical measurements

Four types of electrolytes were prepared, including 1 M calcium bis(trifluoromethanesulfonyl)imide ($Ca(TFSI)_2$) in G_4, 1 M calcium bis(fluorosulfonyl)imide ($Ca(FSI)_2$) in G_4, 1 M calcium tetrafluoroborate ($Ca(BF_4)_2$) in G_4 and 6.25 M $Ca(TFSI)_2$ in deionized water. CR2032 coin cells were assembled using the PTPAn as working electrode and the commercial AC as counter/reference electrodes. The separator was a glass fiber membrane (GF-D, Whatman) with a thickness of 675 μm and a pore diameter of 2.7 μm. Non-aqueous batteries were assembled in a glove box where the content of O_2 and H_2O is below 0.1 ppm. The amount of electrolyte in each cell was 140 μL. The cyclic stability tests were conducted by a Neware battery testing system (CT-4008T). Cyclic voltammetry (CV) measurements were performed by the BioLogic electrochemical workstation (VSP). The potential of Ag/Ag^+ electrode was calibrated by a Fc/Fc^+ redox couple and used to determine the voltage of AC vs. Ca/Ca^{2+}. The electrochemical performance of batteries was conducted in environmental chambers at different temperatures (50, 25, 0, -25 ^oC). The temperature variation during the test was controlled to be less than 1 ^oC. The electrochemical stability window of aqueous electrolytes was determined by LSV in a three-electrode system, in which stainless-steel serves as the working electrode, Pt foil as the counter electrode and SCE as the reference electrode. The area of the working electrode is 1.13 cm^2. Electrochemical impedance spectroscopy (EIS, from 10^5 to 10^{-1} Hz and potential amplitude of 5 mV) of stainless steel/stainless steel cells was conducted to determine ionic conductivities of electrolytes. The ionic conductivities are calculated according to $\sigma = L/A*R$, where R is the measured resistance, L represents the distance between the electrodes and A is the area of the electrodes. The electrochemical tests were repeated under the same condition to verify the reproducibility of the results.

2.5. Computational details

Periodic density functional theory (DFT) calculations were performed in VASP code [52,53]. Generalized gradient approximation (GGA) with the Perdew-Burke-Ernzerhof (PBE) flavor [54] was used. For geometry optimization, the plane-wave cut-off energy of 500 eV was set. The Brillouin-zone was sampled using 3×2×1 k-points grid. The convergence criteria for energy and force were set to be 10^{-5} eV and 0.01 eV $Å^{-1}$, respectively. The van der Waals interaction was considered by using the DFT-D3 [55] approach. The climbing image nudged elastic band (CI-NEB) method [56] was applied to calculate the diffusion energy barriers. Ab initio molecular dynamics (AIMD) simulations [57] with NVT ensemble were performed at 300 K with the time step of 2 fs.

The binding energy of anion X^- incorporated into PTPAn was defined as:

$$E_b = E(PTPAn[X_m]) - E(PTPAn[X_{m-1}]) - E(X^-) \qquad (1)$$

Desolvation energies E_{desolv} were calculated in ORCA package [58]. The geometric optimization, single-point energies and solvation energies were calculated under the B3LYP-D3BJ/6-311G*, B2PLYP-D3BJ/def2-TZVP and M06-2X/6-31G* levels, respectively [59-64]. Implicit solvent model was included in the calculations [65].

The inserted voltage of anion X^- versus Ca/Ca^{2+} was calculated by:

$$V_{ins} = \frac{E(PTPAn[X]_m)-E(PTPAn[X]_{m-1})-[E_{gas}(CaX_2)-E(Ca)]/2+E_{desolv}(X^-)}{e} \tag{2}$$

where m is the number of inserted anions, $E(PTPAn[X]_m)$, $E_{gas}(CaX_2)$ and $E(Ca)$ represent the energies of PTPAn with anions inserted, gas-phase CaX_2, Ca atom in the most stable bulk phase, respectively, and e represents elementary charge.

3. Results and discussion

3.1. The anion effect on the electrochemical performance of PTPAn

PTPAn is fabricated by the chemical oxidation polymerization of monomer triphenylamine (TPA) employing ferric chloride ($FeCl_3$) as a Lewis acid catalyst in chloroform ($CHCl_3$). The optimized quasi-2D PTPAn structures consist of TPA units that are linked with each other by para-substitution. In a TPA unit, three benzene rings are rotated in different planes, exhibiting a distorted structure instead of a flat 2D one, as revealed by the density functional theory (DFT) structural relaxation with a conjugate gradient algorithm (Fig. 1a). To further investigate the thermal stability of PTPAn system, the ab initio molecular dynamics (AIMD) simulations with Nose´–Hoover thermostat for NVT ensemble are performed at 300 K with a time step of 2 fs and the total simulation time is set as 15 ps. No obvious structural reconstructions are noticed as the total energy of the system oscillates around the equilibrium values after the equilibrium time, indicating its stability at room temperature (Fig. S2). Fourier transform infrared spectroscopy (FTIR) spectra detect a new peak at 819 cm^{-1} attributed to C-H out-of-plane vibration after reaction, verifying the formation of 1,4-disubstituted benzene rings and the successful polymerization of TPA units (Fig.

S3a) [66]. Raman spectroscopy is conducted to further examine the structure of PTPAn. The characteristic peaks of the mono-substituted rings of TPA at 1001 and 1033 cm^{-1} almost disappear after polymerization, indicating the formation of PTPAn (Fig. S3b) [67]. The polymer shows a porous structure consisting of microsized sheets (Fig. S4). X-ray diffraction (XRD) patterns with a broad peak at 18^o (2θ) demonstrate the amorphous nature of as-synthesized PTPAn (Fig. S5a), which is further confirmed by the electron diffraction pattern (Fig. S6).

As an anion storage material, the anion categories would highly affect the storage behavior and electrochemical performance of the PTPAn. Three commercially available salts, i.e., $Ca(BF_4)_2$, $Ca(FSI)_2$ and $Ca(TFSI)_2$, are selected to investigate the anion effect because of their relatively high solubility that is essential to achieving high energy density in dual ion batteries. G_4 is selected as the solvent since the Ca^{2+} intercalation in graphite anode is only possible with solvent co-intercalation under several special electrolytes, where the G_4-based one shows a wide electrochemical window for building high-voltage cells (Fig. S7) [27,28]. The performance of PTPAn in $Ca(BF_4)_2$, $Ca(FSI)_2$ and $Ca(TFSI)_2$ electrolytes are compared in Fig. 1b. PTPAn delivers the best performance in $Ca(TFSI)_2$ electrolyte, i.e., capacity retention of 88% at 50C (with respect to the value at 1C), and 82% after 2000 cycles (Fig. S8-12). By sharp contrast, $Ca(BF_4)_2$-based one only maintains 13% and 41% (after 300 cycles) under the same conditions.

The above observations prove the remarkable effect of anions and pose a question about which anion properties account for such a huge distinction. We first examine the electrolyte properties. The comparable ionic conductivities of three electrolytes indicate mass transfer has a negligible effect on the performance difference (Fig. 1c and Fig. S13). We then explore the diffusion difference of anions in PTPAn by measuring diffusion coefficients (galvanostatic intermittent titration technique) and calculating diffusion energy barriers through DFT calculations (Fig. 1d and Fig. S14). $TFSI^-$ anion delivers the highest diffusion coefficient and lowest energy barrier, which is possibly responsible for the superior rate performance of PTPAn in $Ca(TFSI)_2$-G_4 electrolyte. Besides the anion diffusion, the associating process between anions and PTPAn would also affect the kinetics. As shown in Fig. 1e, the binding energies of $PTPAn^+{\cdot}TFSI^-$, $PTPAn^+{\cdot}FSI^-$, and $PTPAn^+{\cdot}BF_4^-$ are calculated to be -2.13, -2.32 and -3.71 eV, respectively. This indicates that the release of BF_4^- from the PTPAn is very tough compared with $TFSI^-$ and FSI^-, leading to poor cyclic stability [68]. In short, $TFSI^-$ anion enables the best performance owing to the fast diffusion process and low binding energy.

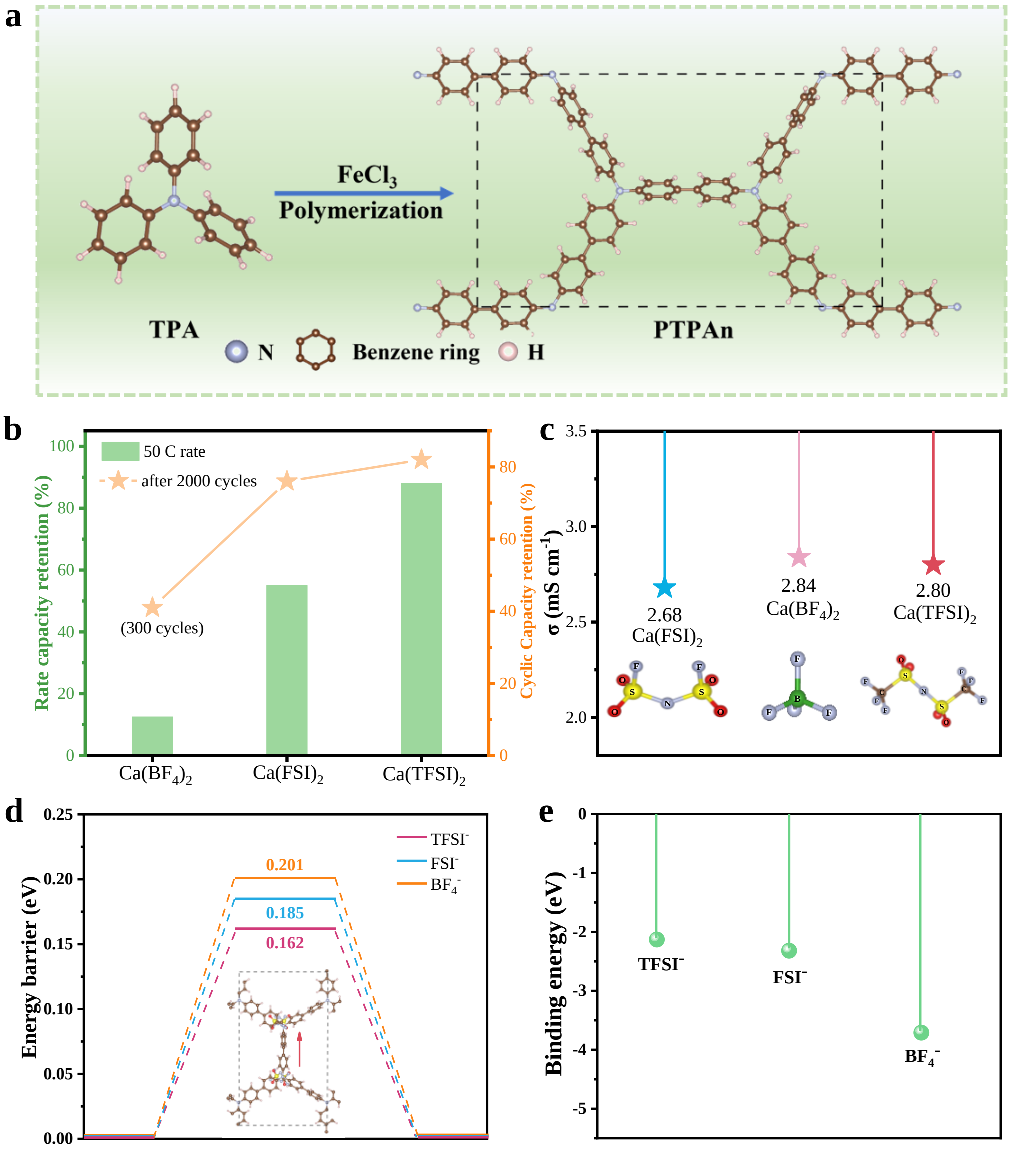

Fig. 1. The anion effect on the performance of PTPAn cathode. (a) Schematic illustration of the polymerization process of TPA. (b) The comparison on cycle life and rate performance of PTPAn in different electrolytes. (c) The comparison of ionic conductivity of three electrolytes. (d) Calculated diffusion energy barriers of anions in PTPAn. (e) Calculated binding energies between anions and PTPAn.

3.2. Electrochemical behavior of PTPAn in $Ca(TFSI)_2$-G_4 electrolytes

We then focus on $Ca(TFSI)_2$-G_4 electrolytes to systematically investigate the electrochemical behavior of PTPAn. The water content in the electrolyte is 41 ppm, as determined by the Karl-Fischer method. Activated carbon (AC) is employed as counter/reference electrodes due to the irreversible Ca plating/stripping in common electrolytes. The voltage of AC electrode is calibrated by a ferrocene/ferrocenium (Fc/Fc^+) redox couple to be around 3.1 V vs. Ca/Ca^{2+} (Fig. S15) [39]. As shown in Fig. 2a, the PTPAn cathode delivers a specific capacity of 88 mAh g^{-1} with an initial CE of 80% and rapid increase to 99%, indicating excellent reversibility. The slightly low initial CE should be due to the minor amount of electrolyte decomposition and irreversible $TFSI^-$ stored in PTPAn during the first cycle, as revealed by the S 2p X-ray photoelectron spectrometry (XPS) spectrum where a weak S signal presents in the fully discharged PTPAn (Fig. S16a). Besides, other irreversible reactions may occur, including further electro-polymerization of the TPA oligomer [69]. The sloping voltage profiles of the PTPAn cathode exhibit an average discharge potential of 3.8 V vs. Ca/Ca^{2+} (Fig. 2b). The rate performance of the PTPAn cathode is investigated by increasing the specific currents from 0.1 to an ultra-high value of 10 A g^{-1}, corresponding to about 100C rate (Fig. 2c). The discharge capacity remains almost the initial value without any loss from 0.1 to 1 A g^{-1}. When the specific current further increases to 2, 3, 5 and 10 A g^{-1}, the PTPAn delivers specific capacities of 86, 85, 77 and 55 mAh g^{-1}, respectively, suggesting a prominent rate performance and fast anion diffusion in the cathode.

The reaction kinetics of the PTPAn cathode is explored by cyclic voltammetry (CV) measurement under different scan rates (v) from 0.2 to 1 mV s^{-1} (Fig. 2f). The CV curves consist of two pairs of peaks at around 3.77/3.66 and 4.09/3.99 V vs. Ca/Ca^{2+}, corresponding to the $TFSI^{-}$ storage in the two N sites, which will be discussed later. The relationship between the peak current (i) and v is fitted with the formula of $i = av^b$, where a and b are constants for probing the reaction kinetics. A b value of around 0.5 reveals a diffusion-controlled process, while the b value approaching 1 signifies a pseudo-capacitive controlled behavior [70]. As shown in Fig. 2g, the b values of all peaks are greater than 0.9, indicating a pseudo-capacitive characteristic that explains the fast diffusion of anions in the PTPAn cathode. The pseudo-capacitive contribution in the total capacity is determined by $i = k_1v+k_2v^{1/2}$, where k_1v represent pseudo-capacitive process and $k_2v^{1/2}$ is diffusion-controlled process. As shown in Fig. S17, the pseudo-capacitive contribution ratios of the PTPAn cathode increase from 93.6% to 97.0% with the scan rate rising from 0.2 to 1.0 mV s^{-1}, further reflecting that the pseudo-capacitive contribution holds dominant position. The long-term cyclic stability of the PTPAn cathode is verified under a large specific current of 1 A g^{-1} at 25 ^{o}C (Fig. 2d). It is a delight to find that a stable electrode/electrolyte interface is presented, as evidenced by the nearly unchanged interfacial resistance before and after cycling (Fig. S18). The electrode delivers a reversible capacity of 67 mAh g^{-1} after 2000 cycles, corresponding to a capacity retention of 82%, which is rarely achieved in other reported cathodes (Table S1).

Realizing low-temperature operation for available inorganic cathodes remains challenging due to the sluggish kinetics caused by the low Ca^{2+} diffusion coefficient.

On the contrary, the PTPAn cathode undergoes an anion-hosting reaction assuring fast reaction kinetics, which makes it possible for working at low temperatures. As shown in Fig. 2e, the PTPAn cathode provides a comparable capacity and excellent stability at 0 ^{o}C as that at 25 ^{o}C. Excitingly, at -25 ^{o}C, it can still deliver a specific capacity of 80 mAh g^{-1} at 0.1 A g^{-1} and stably run for over 300 cycles. A superior cycling performance at 50 ^{o}C is also demonstrated, making the PTPAn a potential cathode for wide-temperature CDIBs. Fig. 2h and Table S1 summarize the performance of the state-of-the-art reported cathodes for Ca-based batteries, where the PTPAn cathode shows the best overall performance considering the cyclic stability, specific capacity, average voltage, and rate capability.

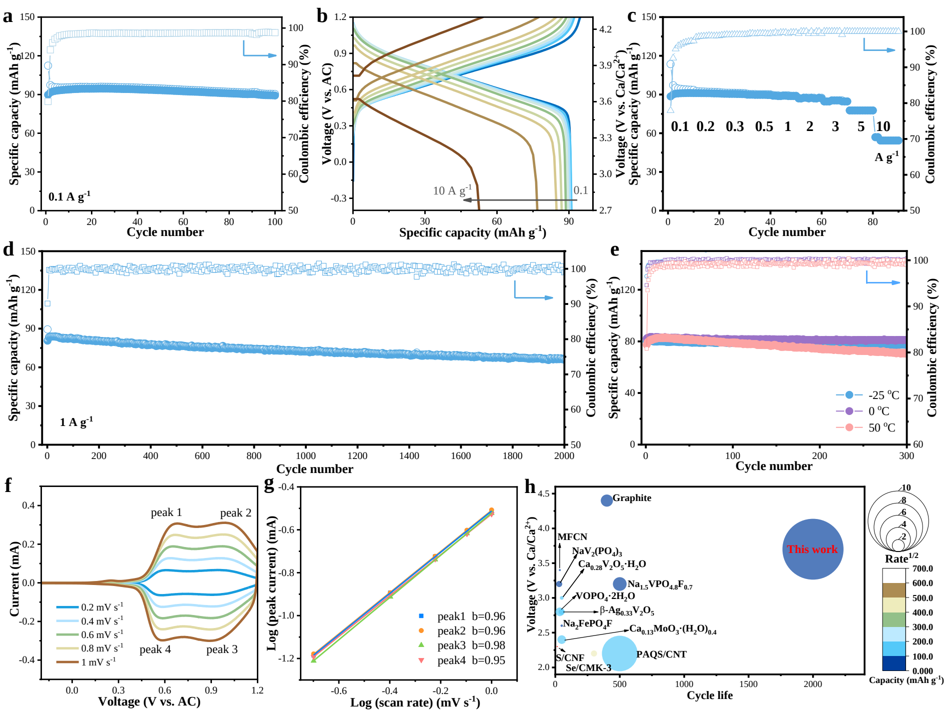

Fig. 2. Electrochemical performance of PTPAn in Ca(TFSI)$_2$-G$_4$ electrolyte. (a) Cycling performance at 0.1 A g^{-1}. (b) Voltage profiles and (c) rate performance under different specific currents. Long-term cyclic stability at (d) 25 ^{o}C and (e) -25, 0 and 50 ^{o}C. (f) CV curves at various scan rates. (g) The b-values fitted by the peak current and scan rate. (h) Comparison with reported cathodes in terms of cycle life, average discharge voltage, specific capacity and highest rate. The reproduxibility of the results has been confirmed by repeated tests under the same condition.

Considering the superior electrochemical performance of the PTPAn cathode, it is of great significance to investigate the underlying reaction mechanism. The electrostatic potential (ESP) distribution on a van der Waals surface can be used to estimate the active sites for electrochemical reactions. Based on Fig. 3a, the ESP value at the N center exhibits the most positive distribution (isosurface level set as 55 eV/Å^3) in the whole system, which means that the nucleophiles are more likely to bind near the N center [71]. Ex-situ Raman spectra of the PTPAn cathode are collected at different discharge/charge states (Fig. 3b). As shown in Fig. 3c, three peaks at 1175, 1288 and 1606 cm^{-1} correspond to C-H bending vibration, C-N stretching and C=C ring stretching in the pristine PTPAn [72]. Upon charging, a new peak assigned to SO_2 asymmetric stretching in $TFSI^-$ anions appears at about 1320 cm^{-1}, which becomes more intense with the increase in the charging depth [73]. At the same time, the peak intensity at 1606 cm^{-1}, corresponding to C=C stretching of benzene ring, gradually decreases. A new peak located at 1570 cm^{-1} appears and grows with charging depth, which is associated with the formation of quinoid ring during charge process [74]. A reversible structural evolution is detected during discharging. The characteristic peak of $TFSI^-$ at 1320 cm^{-1} disappears and the peak at 1606 cm^{-1} recovers its original intensity when fully discharged owing to the release of $TFSI^-$. The observation is confirmed by ex-situ FTIR (Fig. 3d). Specifically, increased intensities are detected for the new $C=N^+$ (1550 cm^{-1}) and SO_2 asymmetric vibration ($\nu_a SO_2$, 1349 cm^{-1}) during charging, revealing the formation of the charged $C=N^+$ and following combination with $TFSI^-$ in PTPAn [75,76]. Meanwhile, the peak at 1515 cm^{-1} indicates the formation of the quinoid structure. The characteristic peak of $TFSI^-$ almost vanish after fully discharging. These results imply a good reversibility of the PTPAn cathode. The existence of the reaction between $TFSI^-$ species and PTPAn is further proved by the solution-state and solid-state ^{19}F NMR spectroscopy, where the charged PTPAn cathode shows an obvious signal at about -79.2 ppm corresponding to $TFSI^-$ anion (Fig. S19).

We employ ex-situ XPS to further probe the redox chemistry of the PTPAn cathode at different electrochemical states. A peak at 400 eV corresponding to the C-N bond is detected in N 1s XPS spectrum of the initial PTPAn (Fig. 3e). With continuous charging, a new peak with increased intensity is observed at 401.5 eV, assigned to the formation of the $TFSI^-/C=N^+$ compound. During discharging, this peak gradually becomes weaker and almost disappears due to the reduction of $C=N^+$ and the release of $TFSI^-$ from the PTPAn cathode. The S 2p and F 1s high-resolution spectra show a similar tendency, further confirming the $TFSI^-$ species in the PTPAn cathode (Fig. S16). The $TFSI^-/C=N^+$ in N 1s and S 2p signals are also detected after surface etching for 100 s, indicating that the reaction not only occurs on the cathode surface (Fig. S20). This observation agrees with the Brunauer-Emmett-Teller result indicating that PTPAn has a low surface area of 36 m^2 g^{-1}, making it hard to sustain a high capacity through surface reaction alone. The $TFSI^-$ capture/release could also be visualized by the elemental mapping of S, which is uniformly distributed on the charged electrode and almost disappears after discharging (Fig. S21). To understand the detailed reaction pathway of the PTPAn, we calculate the reaction potential determined as the Gibbs free energy differences between captured anions and solvated anions. Based on our model, the theoretical voltages of the association between $TFSI^-$ anions and PTPAn are calculated to be 3.63 and 3.96 V, consistent with experimental galvanostatic charge-discharge (GCD) and dQ/dV curves (Fig. 3f).

The reaction mechanism of the PTPAn cathode has been confirmed by the above theoretical calculation and experimental characterizations, which are based on the electron loss/acceptance of N active centers in the PTPAn structure (Fig. 3g). $TFSI^-$ can be associated with the $C=N^+$ generated in PTPAn during the oxidation process and released in the following reduction process, accompanied by the reduction of

$C=N^+$ back to C-N. The CV curves of the PTPAn deliver two pairs of peaks (Fig. 2f). It is mainly associated with the formation of dimer by two TPA units in PTPAn. During the charging process, one of the TPA units first loses an electron to form a $C=N^+$. The neighboring TPA unit subsequently loses another electron at a higher potential owing to the conjugation effects, resulting in the two redox couples in the CV curves [77,78].

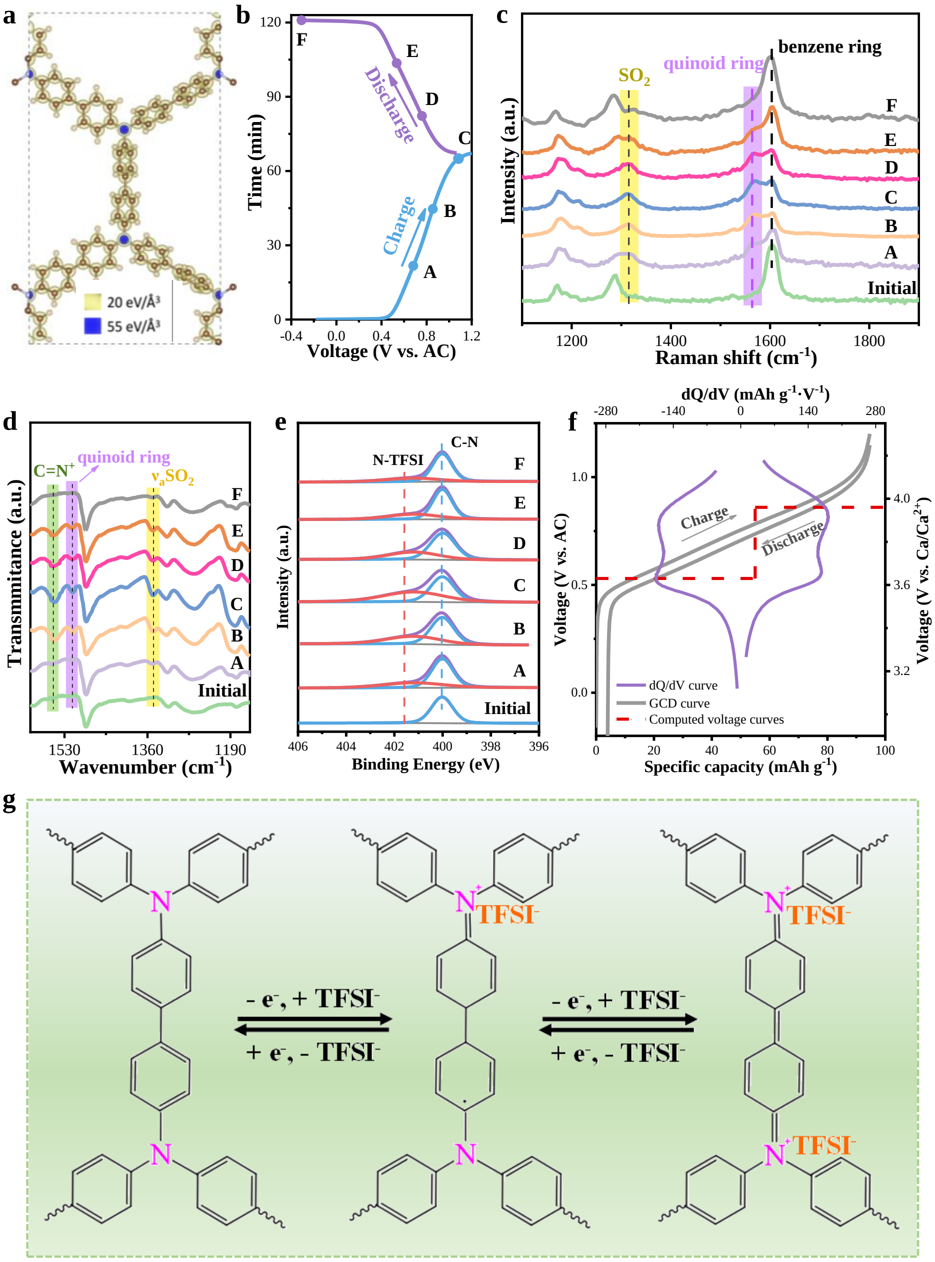

Fig. 3. Reaction mechanism. (a) Calculated ESP map of the PTPAn. Isosurface level: yellow (20 eV/Å^3), blue (55 eV/Å^3). (b) The voltage profile in Ca(TFSI)$_2$-G$_4$ electrolyte. We mark the charge/discharge states at which the ex-situ FTIR patterns, Raman spectra and XPS patterns are collected. Ex-situ (c) Raman spectra, (d) FTIR spectra and (e) N 1s XPS spectra at selected potentials. (f) The calculated theoretical voltage, experimental GCD curve and dQ/dV curve of PTPAn with 1 M Ca(TFSI)$_2$-G$_4$ electrolyte. (g) Reaction mechanism of PTPAn.

3.3. Construction of a full cell

To achieve a high-voltage battery system, a graphite|PTPAn CDIB is constructed due to the low potential (0.7 V vs. Ca/Ca^{2+}) of the graphite anode (Fig. 4a and Fig. S22) [27]. The voltage profiles of the PTPAn cathode, graphite anode and full cell are shown in Fig. 4b. The full cell delivers an average voltage of 2.45 V with a reversible capacity of 72 mAh g^{-1} at 0.3 A g^{-1}. Besides, it presents a remarkable rate capability, as evidenced by high-capacity retention of 72% at 5 A g^{-1} (~50C rate), corresponding to about a half-minute charge/discharge period (Fig. 4c and d). Furthermore, such a full cell also exhibits outstanding cycling performance at both 25 and 0 ^{o}C (Fig. 4e), where reversible capacities of 44 and 40 mAh g^{-1} are achieved after 2000 cycles at a large specific current of 2 A g^{-1}, respectively. It is noted that there is a gradual capacity raising in the initial several cycles caused by the activation of the electrodes at 0 ^{o}C. The prominent performance is among the best compared to other full cells (Table S2), confirming the superiority of the graphite|PTPAn full cell with excellent rate performance and long cycle life.

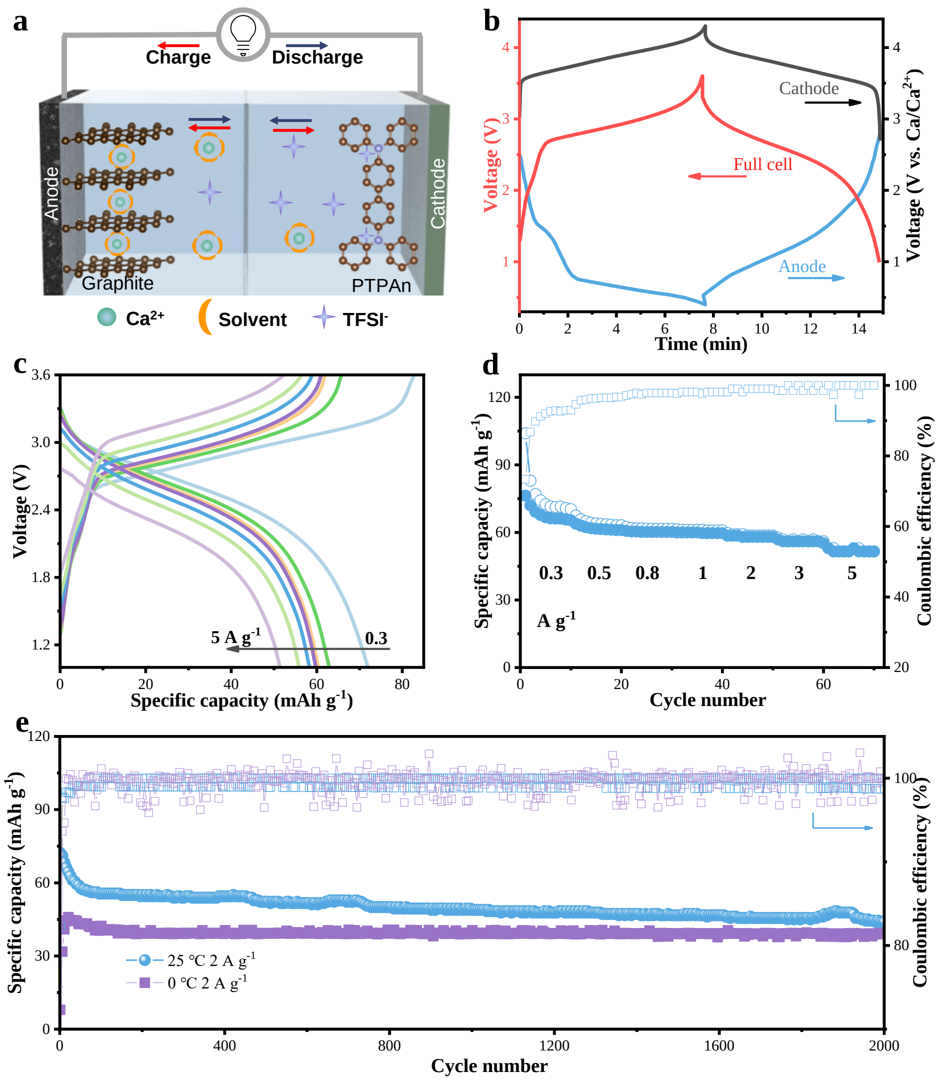

Fig. 4. The graphite|PTPAn full cell in Ca(TFSI)$_2$-G$_4$ electrolyte. (a) Schematic illustration of the full cell. (b) Voltage profiles of the PTPAn, graphite vs. Ca/Ca^{2+} and the full cell. (c) Voltage profiles and (d) rate performance under different specific currents (0.3, 0.5, 0.8, 1, 2, 3 and 5 A g^{-1}). (e) Cycling performance under 2 A g^{-1} at 25 and 0 °C. The capacities are based on the mass of the cathode and the N/P ratio is 2.6. The reproducibility of the results has been confirmed by repeated tests under the same conditions.

3.4. Exploration in aqueous system

Considering the exceptional performance of the PTPAn cathode, we extend the research to the aqueous electrolytes for building high-safety aqueous Ca-based batteries, which attract rising attention recently [79-82]. We first expand the electrochemical window of the aqueous electrolyte to 2.2 V by using a high concentration electrolyte 6.25 M $Ca(TFSI)_2$-H_2O, which can satisfy the operation of the PTPAn cathode and 3,4,9,10-perylene-tetracarboxylic-diimide (PTCDI) anode (Fig. S23). The electrochemical behavior of the PTPAn is explored in half-cells with AC as the counter/reference electrode, which is calibrated to be ~3.28 V vs. Ca/Ca^{2+} using saturated calomel electrode (Fig. S24). As depicted in Fig. 5a, the PTPAn cathode delivers similar discharge/charge profiles and comparable capacity (88 mAh g^{-1} at 0.3 A g^{-1}) with that in organic electrolytes, indicating the same reaction pathway in the two electrolytes. The PTPAn cathode provides appreciable specific capacities of 88, 86, 79, 70 and 54 mAh g^{-1} as specific current increases to 0.5, 1, 2, 3 and 5 A g^{-1}, respectively (Fig. 5a and Fig. S25). In addition, PTPAn also exhibits decent cyclic stability in aqueous electrolyte (Fig. 5b).

To demonstrate its practical aspect, a PTCDI anode is employed to couple with the PTPAn cathode to fabricate an aqueous full cell (Fig. 5c). The PTCDI anode delivers a specific capacity of 105 mAh g^{-1} and excellent cycle stability in the aqueous system (Fig. S26). As shown in Fig. 5d, the full cell provides a stable discharge capacity of 75 mAh g^{-1} with an output voltage of 0.75 V at a specific current of 0.1 A g^{-1}. The increasing capacity and CE in the initial cycles are likely to arise from the activation process of the PTCDI anode (Fig. S26a).

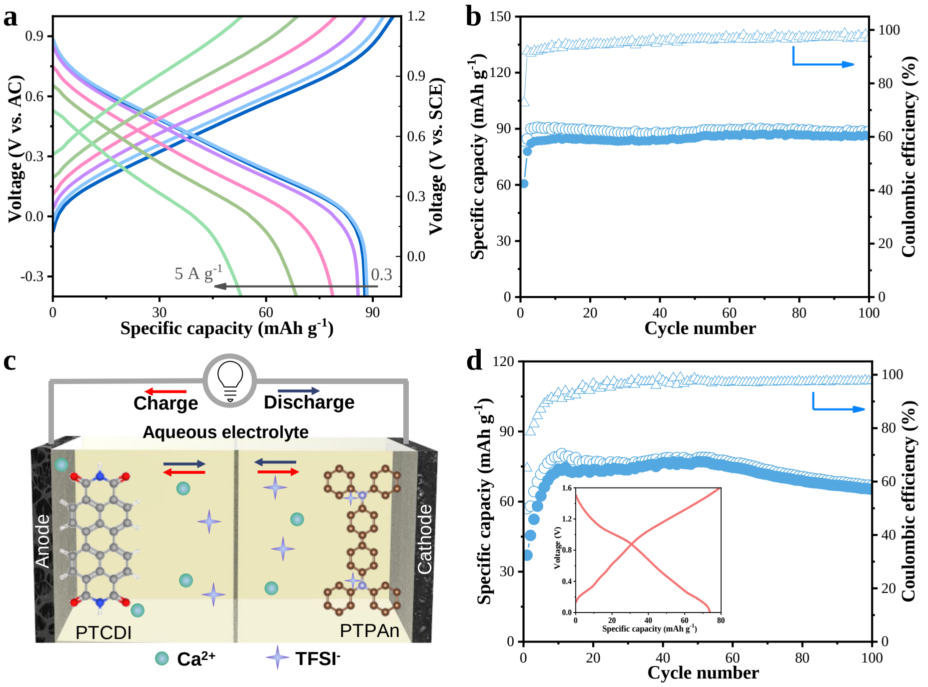

Fig. 5. Electrochemical performance in aqueous system. (a) Voltage profiles of PTPAn under different specific currents. (b) Cyclic performance at 1 A g^{-1}. (c) Schematic illustration of the PTCDI|PTPAn full cell. (d) The cyclic performance and voltage profile (inset) of the full cell at 0.1 A g^{-1}. The N/P ratio of the full cell is 1.1.

4. Conclusions

In summary, an ultra-stable and high-rate CDIB is demonstrated with the assistance of an organic anion-hosting PTPAn cathode. Mechanistic studies with spectroscopic investigations and theoretical calculations confirm that the reaction mechanism of the PTPAn is based on the reversible redox process between C-N and C=N$^+$, accompanied by the combination/release of anions in the PTPAn. More importantly, the anion effect on the electrochemical performance of PTPAn are clarified. Owing to the rapid diffusion and moderate binding of $TFSI^-$ anion in/with PTPAn, $Ca(TFSI)_2$-G_4 electrolyte enables the best rate capability and cyclic stability, i.e., capacity retention of 88% at 50C (with respect to the value at 1C), and 82% after 2000 cycles. The assembled graphite|PTPAn full cell delivers a specific capacity of 72 mAh g^{-1} at 0.3 A g^{-1} with an output voltage of 2.45 V. It also provides an excellent rate capability (capacity retention of 72% at 5 A g^{-1} vs. the capacity at 0.3 A g^{-1}) and long cycle life (2000 cycles). Furthermore, the PTPAn cathode shows outstanding electrochemical performance in the aqueous electrolyte. A high-safety all-organic aqueous CDIB is demonstrated by coupling with a PTCDI anode. This work provides an alternative pathway toward high-rate and ultra-stable Ca-based batteries and a feasible direction to regulate the performance of CDIBs, which would also benefit other metal ion batteries relying on anion storage.

Acknowledgments

R. Z., Z. H. and K.F. contributed equally to the paper. This work was supported by the General Research Fund (GRF) scheme of the Hong Kong Research Grants Council (Project No. 15306422) and the Hong Kong Polytechnic University (ZE2F). We thank Prof. Mingxue Tang and Ms. Jie Liu for the assistance in NMR test.

References

[1] A. Massaro, A.B. Munoz-Garcia, P. Maddalena, F. Bella, G. Meligrana, C. Gerbaldi, M. Pavone, First-principles study of na insertion at tio(2) anatase surfaces: New hints for na-ion battery design, Nanoscale Adv 2 (2020) 2745-2751.

[2] S. Trano, F. Corsini, G. Pascuzzi, E. Giove, L. Fagiolari, J. Amici, C. Francia, S. Turri, S. Bodoardo, G. Griffini, F. Bella, Lignin as polymer electrolyte precursor for stable and sustainable potassium batteries, ChemSusChem 15 (2022) e202200294.

[3] E. Manarin, F. Corsini, S. Trano, L. Fagiolari, J. Amici, C. Francia, S. Bodoardo, S. Turri, F. Bella, G. Griffini, Cardanol-derived epoxy resins as biobased gel polymer electrolytes for potassium-ion conduction, ACS Appl Polym Mater 4 (2022) 3855-3865.

[4] F. Guell, A. Cabot, S. Claramunt, A.O. Moghaddam, P.R. Martinez-Alanis, Influence of colloidal au on the growth of zno nanostructures, Nanomaterials (Basel) 11 (2021).

[5] J. Hu, Y. Hong, M. Guo, Y. Hu, W. Tang, S. Xu, S. Jia, B. Wei, S. Liu, C. Fan, Q. Zhang, Emerging organic

electrodes for na-ion and k-ion batteries, Energy Storage Materials 56 (2023) 267-299.

[6] J. Xie, Q. Zhang, Recent progress in multivalent metal (mg, zn, ca, and al) and metal-ion rechargeable batteries with organic materials as promising electrodes, Small 15 (2019) e1805061.

[7] M. Fichtner, K. Edström, E. Ayerbe, M. Berecibar, A. Bhowmik, I.E. Castelli, S. Clark, R. Dominko, M. Erakca, A.A. Franco, A. Grimaud, B. Horstmann, A. Latz, H. Lorrmann, M. Meeus, R. Narayan, F. Pammer, J. Ruhland, H. Stein, T. Vegge, M. Weil, Rechargeable batteries of the future—the state of the art from a battery 2030+ perspective, n/a 2102904.

[8] Y.S. Joe, M.S. Kang, G. Jang, S.J. Lee, P. Nakhanivei, S.H. Baek, Y.K. Kim, G. Jeong, H.-s. Kim, H.S. Park, Intercalation of bilayered v2o5 by electronically coupled pedot for greatly improved kinetic performance of magnesium ion battery cathodes, Chemical Engineering Journal 460 (2023).

[9] X. Zhang, D. Li, Q. Ruan, L. Liu, B. Wang, F. Xiong, C. Huang, P.K. Chu, Vanadium-based cathode materials for rechargeable magnesium batteries, Materials Today Energy 32 (2023).

[10] Y. Liang, H. Dong, D. Aurbach, Y. Yao, Current status and future directions of multivalent metal-ion batteries, Nature Energy 5 (2020) 646-656.

[11] M.E. Arroyo-de Dompablo, A. Ponrouch, P. Johansson, M.R. Palacin, Achievements, challenges, and prospects of calcium batteries, Chem Rev 120 (2020) 6331-6357.

[12] R.J. Gummow, G. Vamvounis, M.B. Kannan, Y. He, Calcium-ion batteries: Current state-of-the-art and future perspectives, Adv Mater 30 (2018) e1801702.

[13] Z.L. Xu, J. Park, J. Wang, H. Moon, G. Yoon, J. Lim, Y.J. Ko, S.P. Cho, S.Y. Lee, K. Kang, A new high-voltage calcium intercalation host for ultra-stable and high-power calcium rechargeable batteries, Nat Commun 12 (2021) 3369.

[14] S. Kim, L. Yin, M.H. Lee, P. Parajuli, L. Blanc, T.T. Fister, H. Park, B.J. Kwon, B.J. Ingram, P. Zapol, R.F. Klie, K. Kang, L.F. Nazar, S.H. Lapidus, J.T. Vaughey, High-voltage phosphate cathodes for rechargeable ca-ion batteries, Acs Energy Letters 5 (2020) 3203-3211.

[15] S.J.R. Prabakar, W.-B. Park, J.Y. Seo, S.P. Singh, D. Ahn, K.-S. Sohn, M. Pyo, Ultra-stable ti2o(po4)2(h2o) as a viable new ca2+ storage electrode material for calcium-ion batteries, Energy Storage Materials 43 (2021) 85-96.

[16] A. Scafuri, R. Berthelot, K. Pirnat, A. Vizintin, J. Bitenc, G. Aquilanti, D. Foix, R. Dedryvere, I. Arcon, R. Dominko, L. Stievano, Spectroscopic insights into the electrochemical mechanism of rechargeable calcium/sulfur batteries, Chem Mater 32 (2020) 8266-8275.

[17] X.W. Yu, M.J. Boyer, G.S. Hwang, A. Manthiram, Toward a reversible calcium-sulfur battery with a lithium-ion mediation approach, Advanced Energy Materials 9 (2019) 1803794.

[18] Z. Li, B.P. Vinayan, T. Diemant, R.J. Behm, M. Fichtner, Z. Zhao‐Karger, Rechargeable calcium–sulfur batteries enabled by an efficient borate‐based electrolyte, Small 16 (2020) 2001806.

[19] R. Zhou, Z. Hou, Q. Liu, X.Q. Du, J.Q. Huang, B.A. Zhang, Unlocking the reversible selenium electrode for non-aqueous and aqueous calcium-ion batteries, Advanced Functional Materials 32 (2022).

[20] S. Biria, S. Pathreeker, H. Li, I.D. Hosein, Plating and stripping of calcium in an alkyl carbonate electrolyte at room temperature, ACS Applied Energy Materials 2 (2019) 7738-7743.

[21] A. Shyamsunder, L.E. Blanc, A. Assoud, L.F. Nazar, Reversible calcium plating and stripping at room temperature using a borate salt, ACS Energy Letters 4 (2019) 2271-2276.

[22] S. Biria, S. Pathreeker, F.S. Genier, H. Li, I.D. Hosein, Plating and stripping calcium at room temperature in an ionic-liquid electrolyte, ACS Applied Energy Materials 3 (2020) 2310-2314.

[23] A. Ponrouch, C. Frontera, F. Barde, M.R. Palacin, Towards a calcium-based rechargeable battery,

Nat Mater 15 (2016) 169-172.

[24] D. Wang, X. Gao, Y. Chen, L. Jin, C. Kuss, P.G. Bruce, Plating and stripping calcium in an organic electrolyte, Nature Materials 17 (2018) 16-20.

[25] Z.Y. Li, O. Fuhr, M. Fichtner, Z. Zhao-Karger, Towards stable and efficient electrolytes for room-temperature rechargeable calcium batteries, Energy & Environmental Science 12 (2019) 3496-3501.

[26] Z. Zhao-Karger, Y. Xiu, Z. Li, A. Reupert, T. Smok, M. Fichtner, Calcium-tin alloys as anodes for rechargeable non-aqueous calcium-ion batteries at room temperature, Nat Commun 13 (2022) 3849.

[27] S.J. Richard Prabakar, A.B. Ikhe, W.B. Park, K.C. Chung, H. Park, K.J. Kim, D. Ahn, J.S. Kwak, K.S. Sohn, M. Pyo, Graphite as a long-life ca(2+)-intercalation anode and its implementation for rocking-chair type calcium-ion batteries, Adv Sci (Weinh) 6 (2019) 1902129.

[28] J. Park, Z.L. Xu, G. Yoon, S.K. Park, J. Wang, H. Hyun, H. Park, J. Lim, Y.J. Ko, Y.S. Yun, K. Kang, Stable and high-power calcium-ion batteries enabled by calcium intercalation into graphite, Adv Mater 32 (2020) e1904411.

[29] Y. Xiu, A. Mauri, S. Dinda, Y. Pramudya, Z. Ding, T. Diemant, A. Sarkar, L. Wang, Z. Li, W. Wenzel, M. Fichtner, Z. Zhao-Karger, Anion storage chemistry of organic cathodes for high-energy and high-power density divalent metal batteries, Angew Chem Int Ed Engl (2022) e202212339.

[30] B. Ji, H. He, W. Yao, Y. Tang, Recent advances and perspectives on calcium-ion storage: Key materials and devices, Adv Mater 33 (2021) e2005501.

[31] M.S. Chae, H.H. Kwak, S.T. Hong, Calcium molybdenum bronze as a stable high-capacity cathode material for calcium-ion batteries, Acs Applied Energy Materials 3 (2020) 5107-5112.

[32] M.E. Purbarani, J. Hyoung, S.-T. Hong, Crystal-water-free potassium vanadium bronze (k0.5v2o5) as a cathode material for ca-ion batteries, ACS Applied Energy Materials 4 (2021) 7487-7491.

[33] J. Hyoung, J.W. Heo, B. Jeon, S.-T. Hong, Silver vanadium bronze, β-ag0.33v2o5: Crystal-water-free high-capacity cathode material for rechargeable ca-ion batteries, J Mater Chem A 9 (2021) 20776-20782.

[34] B. Jeon, H.H. Kwak, S.-T. Hong, Bilayered ca0.28v2o5·h2o: High-capacity cathode material for rechargeable ca-ion batteries and its charge storage mechanism, Chem Mater 34 (2022) 1491-1498.

[35] C. Lee, Y.-T. Jeong, P.M. Nogales, H.-Y. Song, Y. Kim, R.-Z. Yin, S.-K. Jeong, Electrochemical intercalation of ca2+ ions into tis2 in organic electrolytes at room temperature, Electrochemistry Communications 98 (2019) 115-118.

[36] M. Cabello, F. Nacimiento, R. Alcántara, P. Lavela, C. Pérez Vicente, J.L. Tirado, Applicability of molybdite as an electrode material in calcium batteries: A structural study of layer-type caxmoo3, Chem Mater 30 (2018) 5853-5861.

[37] M.S. Chae, J.W. Heo, J. Hyoung, S.-T. Hong, Double-sheet vanadium oxide as a cathode material for calcium-ion batteries, ChemNanoMat 6 (2020) 1049-1053.

[38] X. Xu, M. Duan, Y. Yue, Q. Li, X. Zhang, L. Wu, P. Wu, B. Song, L. Mai, Bilayered mg0.25v2o5·h2o as a stable cathode for rechargeable ca-ion batteries, ACS Energy Letters 4 (2019) 1328-1335.

[39] B. Jeon, J.W. Heo, J. Hyoung, H.H. Kwak, D.M. Lee, S.T. Hong, Reversible calcium-ion insertion in nasicon-type nav2(po4)(3), Chem Mater 32 (2020) 8772-8780.

[40] A.L. Lipson, S. Kim, B. Pan, C. Liao, T.T. Fister, B.J. Ingram, Calcium intercalation into layered fluorinated sodium iron phosphate, Journal of Power Sources 369 (2017) 133-137.

[41] T. Tojo, H. Tawa, N. Oshida, R. Inada, Y. Sakurai, Electrochemical characterization of a layered α-moo3 as a new cathode material for calcium ion batteries, Journal of Electroanalytical Chemistry

825 (2018) 51-56.

[42] N. Kuperman, P. Padigi, G. Goncher, D. Evans, J. Thiebes, R. Solanki, High performance prussian blue cathode for nonaqueous ca-ion intercalation battery, Journal of Power Sources 342 (2017) 414-418.

[43] A.L. Lipson, B.F. Pan, S.H. Lapidus, C. Liao, J.T. Vaughey, B.J. Ingram, Rechargeable ca-ion batteries: A new energy storage system, Chem Mater 27 (2015) 8442-8447.

[44] M.E.A.-d. Dompablo, C. Krich, J. Nava-Avendaño, N. Biškup, M.R. Palacín, F. Bardé, A joint computational and experimental evaluation of camn2o4 polymorphs as cathode materials for ca ion batteries, Chem Mater 28 (2016) 6886-6893.

[45] M. Cabello, F. Nacimiento, J.R. González, G. Ortiz, R. Alcántara, P. Lavela, C. Pérez-Vicente, J.L. Tirado, Advancing towards a veritable calcium-ion battery: Caco2o4 positive electrode material, Electrochemistry Communications 67 (2016) 59-64.

[46] T. Placke, A. Heckmann, R. Schmuch, P. Meister, K. Beltrop, M. Winter, Perspective on performance, cost, and technical challenges for practical dual-ion batteries, Joule 2 (2018) 2528-2550.

[47] M. Wang, C. Jiang, S. Zhang, X. Song, Y. Tang, H.M. Cheng, Reversible calcium alloying enables a practical room-temperature rechargeable calcium-ion battery with a high discharge voltage, Nat Chem 10 (2018) 667-672.

[48] S. Wu, F. Zhang, Y. Tang, A novel calcium-ion battery based on dual-carbon configuration with high working voltage and long cycling life, Advanced Science 5 (2018) 1701082.

[49] J. Li, C. Han, X. Ou, Y. Tang, Concentrated electrolyte for high-performance ca-ion battery based on organic anode and graphite cathode, Angew Chem Int Ed Engl n/a (2022) e202116668.

[50] J.K. Feng, Y.L. Cao, X.P. Ai, H.X. Yang, Polytriphenylamine: A high power and high capacity cathode material for rechargeable lithium batteries, Journal of Power Sources 177 (2008) 199-204.

[51] B. Jiang, Y. Su, R. Liu, Z. Sun, D. Wu, Calcium based all-organic dual-ion batteries with stable low temperature operability, Small 18 (2022) e2200049.

[52] G. Kresse, J. Furthmüller, Efficient iterative schemes for ab initio total-energy calculations using a plane-wave basis set, Physical review B 54 (1996) 11169.

[53] G. Kresse, D. Joubert, From ultrasoft pseudopotentials to the projector augmented-wave method, Physical review b 59 (1999) 1758.

[54] J.P. Perdew, K. Burke, M. Ernzerhof, Generalized gradient approximation made simple, Physical review letters 77 (1996) 3865.

[55] S. Grimme, J. Antony, S. Ehrlich, H. Krieg, A consistent and accurate ab initio parametrization of density functional dispersion correction (dft-d) for the 94 elements h-pu, The Journal of chemical physics 132 (2010) 154104.

[56] G. Henkelman, B.P. Uberuaga, H. Jónsson, A climbing image nudged elastic band method for finding saddle points and minimum energy paths, The Journal of chemical physics 113 (2000) 9901-9904.

[57] S. Nosé, A unified formulation of the constant temperature molecular dynamics methods, The Journal of chemical physics 81 (1984) 511-519.

[58] F. Neese, The orca program system, Wiley Interdiscip. Rev.: Comput. Mol. Sci. 2 (2012) 73-78.

[59] R. Krishnan, J.S. Binkley, R. Seeger, J.A. Pople, Self‐consistent molecular orbital methods. Xx. A basis set for correlated wave functions, J. Chem. Phys. 72 (1980) 650-654.

[60] W.J. Hehre, R. Ditchfield, J.A. Pople, Self—consistent molecular orbital methods. Xii. Further extensions of gaussian—type basis sets for use in molecular orbital studies of organic molecules, J.

Chem. Phys. 56 (1972) 2257-2261.

[61] V.A. Rassolov, J.A. Pople, M.A. Ratner, T.L. Windus, 6-31g* basis set for atoms k through zn, J. Chem. Phys. 109 (1998) 1223-1229.

[62] Y. Zhao, D.G. Truhlar, The m06 suite of density functionals for main group thermochemistry, thermochemical kinetics, noncovalent interactions, excited states, and transition elements: Two new functionals and systematic testing of four m06-class functionals and 12 other functionals, Theor. Chem. Acc. 120 (2008) 215-241.

[63] S. Grimme, S. Ehrlich, L. Goerigk, Effect of the damping function in dispersion corrected density functional theory, J. Comput. Chem. 32 (2011) 1456-1465.

[64] F. Weigend, R. Ahlrichs, Balanced basis sets of split valence, triple zeta valence and quadruple zeta valence quality for h to rn: Design and assessment of accuracy, Phys. Chem. Chem. Phys. 7 (2005) 3297-3305.

[65] V. Barone, M. Cossi, Quantum calculation of molecular energies and energy gradients in solution by a conductor solvent model, J. Phys. Chem. A 102 (1998) 1995-2001.

[66] J. Chen, Y. Peng, Y. Yin, Z. Fang, Y. Cao, Y. Wang, X. Dong, Y. Xia, A desolvation-free sodium dual-ion chemistry for high power density and extremely low temperature, Angew Chem Int Ed Engl 60 (2021) 23858-23862.

[67] M.I. Boyer, S. Quillard, E. Rebourt, G. Louarn, J.P. Buisson, A. Monkman, S. Lefrant, Vibrational analysis of polyaniline: A model compound approach, J Phys Chem B 102 (1998) 7382-7392.

[68] Y. Luo, F. Zheng, L. Liu, K. Lei, X. Hou, G. Xu, H. Meng, J. Shi, F. Li, A high-power aqueous zinc-organic radical battery with tunable operating voltage triggered by selected anions, ChemSusChem 13 (2020) 2239-2244.

[69] A. Petr, C. Kvarnström, L. Dunsch, A. Ivaska, Electrochemical synthesis of electroactive polytriphenylamine, Synthetic Metals 108 (2000) 245-247.

[70] J. Wang, J. Polleux, J. Lim, B. Dunn, Pseudocapacitive contributions to electrochemical energy storage in tio2 (anatase) nanoparticles, The Journal of Physical Chemistry C 111 (2007) 14925-14931.

[71] P. Sjoberg, P. Politzer, Use of the electrostatic potential at the molecular-surface to interpret and predict nucleophilic processes, J Phys Chem-Us 94 (1990) 3959-3961.

[72] C. Kvarnström, A. Petr, P. Damlin, T. Lindfors, A. Ivaska, L. Dunsch, Raman and ftir spectroscopic characterization of electrochemically synthesized poly(triphenylamine), ptpa, Journal of Solid State Electrochemistry 6 (2002) 505-512.

[73] R. Mazeikiene, G. Niaura, A. Malinauskas, Poly(n-methylaniline) vs. Polyaniline: An extended ph range of polaron stability as revealed by raman spectroelectrochemistry, Spectrochim Acta A Mol Biomol Spectrosc 262 (2021) 120140.

[74] M. Baibarac, L. Mihut, G. Louarn, J.Y. Mevellec, J. Wery, S. Lefrant, I. Baltog, Interfacial chemical effect evidenced on sers spectra of polyaniline thin films deposited on rough metallic supports, 30 (1999) 1105-1113.

[75] J. Bitenc, A. Vizintin, J. Grdadolnik, R. Dominko, Tracking electrochemical reactions inside organic electrodes by operando ir spectroscopy, Energy Storage Materials 21 (2019) 347-353.

[76] S. Xu, H. Dai, S. Zhu, Y. Wu, M. Sun, Y. Chen, K. Fan, C. Zhang, C. Wang, W. Hu, A branched dihydrophenazine-based polymer as a cathode material to achieve dual-ion batteries with high energy and power density, eScience 1 (2021) 60-68.

[77] L. Fan, Q. Liu, Z. Xu, B. Lu, An organic cathode for potassium dual-ion full battery, ACS Energy Letters 2 (2017) 1614-1620.

[78] X. Qiu, N. Wang, X. Dong, J. Xu, K. Zhou, W. Li, Y. Wang, A high-voltage zn-organic battery using a nonflammable organic electrolyte, Angew Chem Int Ed Engl 60 (2021) 21025-21032.

[79] M.S. Chae, A. Nimkar, N. Shpigel, Y. Gofer, D. Aurbach, High performance aqueous and nonaqueous ca-ion cathodes based on fused-ring aromatic carbonyl compounds, ACS Energy Letters 6 (2021) 2659-2665.

[80] S. Gheytani, Y. Liang, F. Wu, Y. Jing, H. Dong, K.K. Rao, X. Chi, F. Fang, Y. Yao, An aqueous ca-ion battery, Adv Sci (Weinh) 4 (2017) 1700465.

[81] C. Han, H. Li, Y. Li, J. Zhu, C. Zhi, Proton-assisted calcium-ion storage in aromatic organic molecular crystal with coplanar stacked structure, Nat Commun 12 (2021) 2400.

[82] X. Tang, D. Zhou, B. Zhang, S. Wang, P. Li, H. Liu, X. Guo, P. Jaumaux, X. Gao, Y. Fu, C. Wang, C. Wang, G. Wang, A universal strategy towards high-energy aqueous multivalent-ion batteries, Nat Commun 12 (2021) 2857.